Tectonics

RESEARCH ARTICLE
10.1029/2020TC006584

Key Points:

- ^{10}Be exposure ages for folded fluvial terraces yield a vertical slip rate of 0.6 ± 0.2 mm/year for the Danghe Nan Shan thrust fault
- The fault geometry derived from the folded terraces combined with fold-area balancing yields a shortening rate of 0.8 ± 0.2 mm/year
- GPS data and fault slip rates suggest ~5 mm/year of NNE–SSW-directed shortening by thrust faulting in the interior of northern Tibet

Supporting Information:

- Supporting Information S1

Correspondence to:
R. Hetzel,
rahetzel@uni-muenster.de

Citation:
Xu, Q., Hetzel, R., Hampel, A., & Wolff, R. (2021). Slip rate of the Danghe Nan Shan thrust fault from ^{10}Be exposure dating of folded river terraces: Implications for the strain distribution in northern Tibet. *Tectonics*, *40*, e2020TC006584. https://doi.org/10.1029/2020TC006584

Received 20 OCT 2020
Accepted 26 FEB 2021

Slip Rate of the Danghe Nan Shan Thrust Fault from ^{10}Be Exposure Dating of Folded River Terraces: Implications for the Strain Distribution in Northern Tibet

Q. Xu[1,2], R. Hetzel[3], A. Hampel[4], and R. Wolff[3]

[1]State Key Laboratory of Oil and Gas Reservoir and Geology Exploration, Chengdu, China, [2]Division of Key Laboratory of Carbonate Reservoirs of CNPC, Southwest Petroleum University, Chengdu, China, [3]Institut für Geologie und Paläontologie, Westfälische Wilhelms-Universität Münster, Münster, Germany, [4]Institut für Geologie, Leibniz Universität Hannover, Hannover, Germany

Abstract The northeastward motion of the Tibetan Plateau along the Altyn Tagh strike-slip fault causes thrust faulting in three parallel mountain ranges (Qilian Shan, Daxue Shan, and Danghe Nan Shan) in the plateau interior, and leads to NNE-directed crustal shortening and plateau growth. While slip rates at the plateau margin (i.e., along the Qilian Shan and the Altyn Tagh fault) are well constrained, rates of thrust faulting and the strain distribution in the plateau interior remain poorly resolved. Here, we use field investigations, a high-resolution DEM, and ^{10}Be exposure dating to quantify the shortening rate across the Danghe Nan Shan thrust fault from fluvial terraces, which are deformed by a growing NNE-vergent anticline. ^{10}Be exposure ages from two terrace levels range from 70 ± 5 to 92 ± 7 ka. When combined with uplift values of 37–68 m along the fold hinge, the ^{10}Be ages yield a mean uplift rate of 0.6 ± 0.2 mm/year. Using the cross-sectional area of the fold and the subsurface geometry of the listric thrust fault, we obtain a shortening rate of 0.8 ± 0.2 mm/year, which is consistent with the rate of elastic strain accumulation recorded by GPS data. Together with published fault slip rates and GPS data, our results indicate that northern Tibet experiences NNE-directed shortening at a rate of ~5 mm/year between the Qaidam Basin and the Hexi Corridor. In the plateau interior, this shortening is accommodated by several range-bounding thrust faults and closely coupled with the eastward decrease in the slip rate of the Altyn Tagh fault.

1. Introduction

The ongoing convergence between India and Asia causes widespread deformation of the Tibetan Plateau (e.g., Styron et al., 2010; Tapponnier and Molnar, 1977; Taylor et al., 2003). In the northern part of the plateau (i.e., north of the Kunlun strike-slip fault), deformation is mainly partitioned into thrust and strike-slip faulting (e.g., Meyer et al., 1998; Zheng et al., 2013a). In contrast to the more easily accessible plateau margins (i.e., the Altyn Tagh fault and the Qilian Shan), where various studies have determined fault slip rates (e.g., Cowgill et al., 2009; Hetzel, 2013 and references therein; Hu et al., 2015; Xiong et al., 2017; Yang et al., 2018), the remote plateau interior remains poorly studied in terms of quantitative constraints on fault slip rates.

In northern Tibet, active thrust faulting and crustal shortening (Figure 1) are kinematically linked to strike-slip motion on the left-lateral Altyn Tagh fault, which is the largest intracontinental strike-slip fault on Earth and constitutes the northern boundary of the Tibetan Plateau. Its slip rate decreases from 8–12 mm/year west of Subei to 1–2 mm/year near its eastern termination (Cowgill et al., 2009; Gold et al., 2009, 2011; Meyer et al., 1998; Seong et al., 2011; Xu et al., 2005; Zhang et al., 2007, 2013b). This decrease occurs largely at the junctions between the Altyn Tagh fault and three NW-SE striking mountain ranges—the Qilian Shan, Daxue Shan, and Danghe Nan Shan (Figure 1) (e.g., Meyer et al., 1998; Xu et al., 2005). All three ranges reach elevations of ~5.5 km and are bounded by thrust faults, which are marked by prominent fault scarps along the NE-facing range flanks and have been interpreted as crustal-scale ramp anticlines growing by repeated earthquakes (e.g., Meyer et al., 1998).

Along the western Qilian Shan, which represents the northeastern margin of the Tibetan Plateau, late Quaternary slip rates of the frontal thrust fault are well constrained at five sites (Figure 1) and fall in the

10.1029/2020TC006584

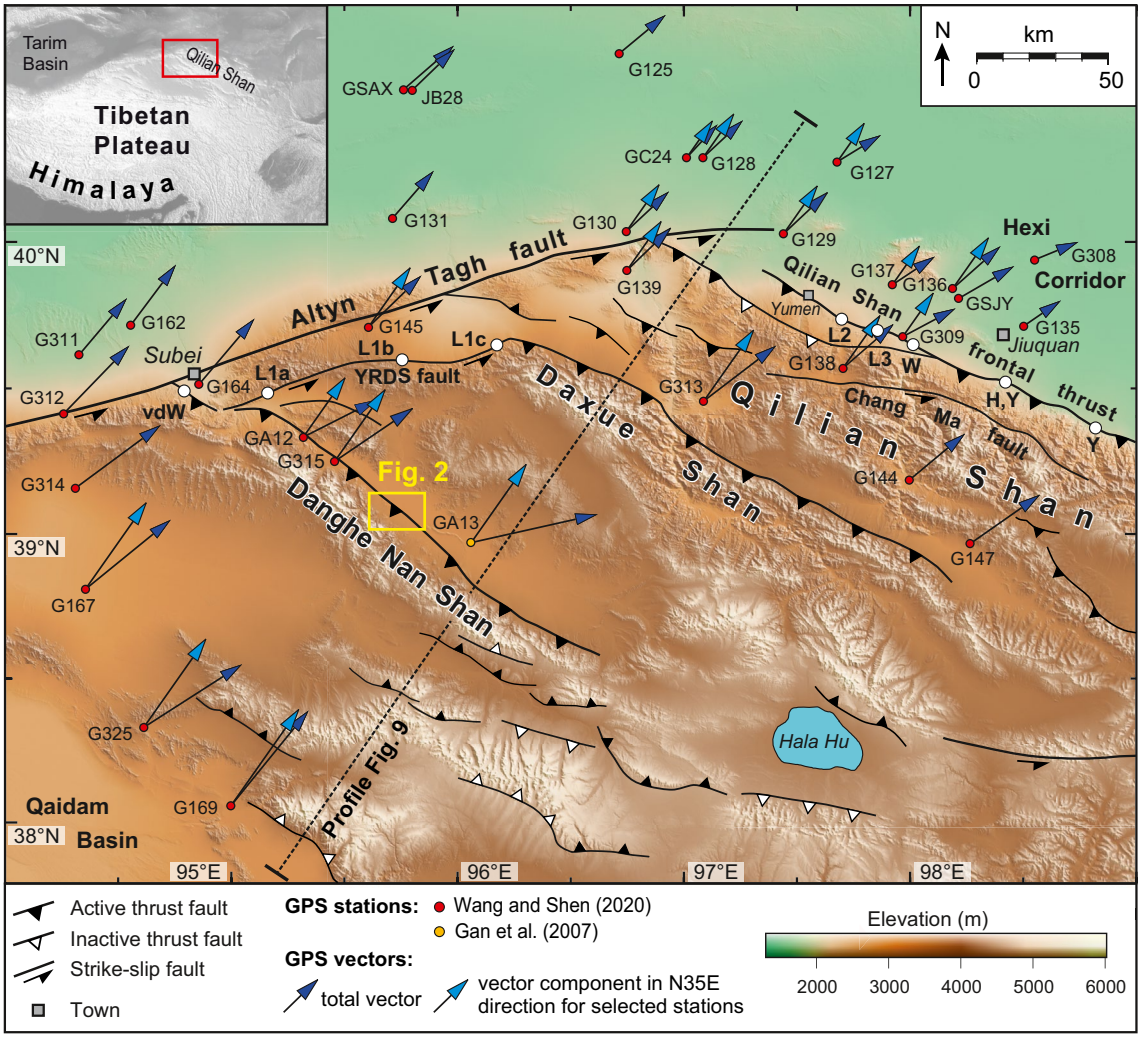

Figure 1. Topographic map of the northeastern Tibetan Plateau with the main active faults. White dots mark the study sites for slip-rate determinations at the major faults. L1a–c: Luo et al. (2015); L2: Liu et al. (2019); L3: Liu et al. (2017a); W: Wang et al. (2020); H: Hetzel et al. (2019); Y, Yang et al. (2018); vdW: van der Woerd et al. (2001). YRDS = Yema River – Daxue Shan strike-slip fault. Yellow box shows study area at the Danghe Nan Shan. The dots and arrows mark GPS sites and their velocity vectors relative to stable Eurasia (Gan et al., 2007; Wang and Shen, 2020). The total velocity and the velocity component perpendicular to the strike of the main thrust faults in the Qilian Shan (i.e., in the direction N35°E) are marked by dark and light blue arrow heads, respectively. The profile line shows the location of the GPS velocity profile in Figure 8.

range of 1.1 ± 0.5 to 2.0 ± 0.3 mm/year (Hetzel et al., 2019; Liu et al., 2017a, 2019; Wang et al., 2020; Yang et al., 2018). At the junctions between the Altyn Tagh fault and the Daxue Shan and Danghe Nan Shan, the slip rate of the Altyn Tagh decreases and slip is transferred onto the thrust faults in the plateau interior (Meyer et al., 1998; Xu et al., 2005; Zhang et al., 2007). In contrast to the Qilian Shan frontal thrust, slip rates of the thrust faults bounding the Daxue Shan and Danghe Nan Shan are poorly constrained. To the best of our knowledge, there is no slip rate available for the Daxue Shan, while the slip rate of the Danghe Nan Shan thrust fault has only been constrained near the Altyn Tagh fault south of Subei (Figure 1). Here, a high Holocene shortening rate of 5.5 ± 1.5 mm/year has been derived from topographic profiles and radiocarbon dating of warped river terraces, which are offset by thrust faults and form fault scarps along the southwestern margin of the Subei Basin (van der Woerd et al., 2001). Whether or not this high rate of SW-NE shortening prevails farther to the southeast along the Danghe Nan Shan is critical for understanding the slip transfer onto thrust faults in the plateau and the distribution of active deformation within the plateau. However, apart from the Subei area, rates of thrust faulting along the Danghe Nan Shan remain unknown.

In this study, we determine the slip rate of the central Danghe Nan Shan thrust fault by ^{10}Be exposure dating and constrain the subsurface geometry of the fault from the shape of folded fluvial terraces. In addition, we use GPS data to determine the short-term deformation rate across the main thrust faults in NE Tibet. Based on our results and previously published fault-slip rates, we discuss the partitioning and distribution of strain between the Altyn Tagh fault and the plateau interior.

2. Geological Setting of the Danghe Nan Shan

The Danghe Nan Shan is one of the largest mountain range in northern Tibet, extending NW-SE over a distance of ~250 km from the Altyn Tagh fault near the town of Subei to the Lake Hala (Figure 1). The range comprises several peaks with elevations around 5000 m, with the highest summit reaching 5672 m above sea level. Northeast of the Danghe Nan Shan lies the intramontane Yanchiwan Basin at an elevation of about 3150 m. The core of the Danghe Nan Shan consists of deformed Paleozoic metasedimentary and plutonic rocks that record an early Paleozoic orogeny and a subsequent phase of Mesozoic extension (Figure 2) (Gansu Geological Bureau, 1975). During Cenozoic mountain building, the Paleozoic rocks were deformed by reverse faults and placed against folded and uplifted Neogene red beds and Quaternary alluvial sediments along the northeastern range front (Figure 2b) (Meyer et al., 1998; van der Woerd et al., 2001).

Satellite images and geologic field observations from the central Danghe Nan Shan show the presence of an active, NW-striking thrust fault that folds and cuts late Quaternary sediments and fluvial terraces on the northeastern side of the range (Meyer et al., 1998; Shao et al., 2010). We refer to this fault as the Danghe Nan Shan frontal thrust (Figure 2). Fault scarps up to several tens of meters high extend over a distance of 17 km along the fault, which has a total length of ~45 km (Shao et al., 2017). Paleoseismic investigations revealed the presence of fresh scarps with an average height of 0.8 ± 0.2 m and a lateral extent of ~14 km, which probably formed during an M_W 7.0 ± 0.5 earthquake in A.D. 1289 (Shao et al., 2017). Another active thrust fault, which we call piedmont thrust fault, is situated 5 km farther to the southwest (Figure 2). Where exposed, this fault dips steeply with an angle of about 70° and thrusts Neogene red beds against Quaternary alluvial gravels (Meyer et al., 1998; Shao et al., 2010). Two river terraces offset by the fault form scarps with a height of 1.5 and 11 m, respectively (Shao et al., 2010).

In this study, we focus on a series of folded fluvial terraces that occur in the central part of the Danghe Nan Shan frontal thrust between the Zhonghong and Xiaohong channels (Figure 2). In the next section, we describe the data and methods employed in our study.

3. Data and Methods

3.1. Topographic Data

The topography of the study area was constrained using a digital elevation model (DEM) derived from two WorldView satellite images (acquisition dates: scene 1020010007CA1A00 on 2 June 2009 (WorldView 1), and scene 1030010012A64D00 on 28 March 2012 (WorldView 2); (c) NextView 2015). The DEM was created using NASA AMES Stereo Pipeline version 2.5.1 (Noh and Howat, 2015) and has a horizontal resolution of 1.5 m and an internal vertical accuracy of ~0.2 m (cf. Shean et al., 2016).

Using the DEM and field observations, we mapped the different terrace levels, stream channels, and fault strands in the study area to determine the spatial relationship between the terraces and the fault scarp (Figure 3). We also extracted eight topographic profiles across the fault scarp (P1–P8) and two stream profiles (Pa and Pb) in order to quantify the vertical uplift related to the thrust-fault scarp (Figure 4), the subsurface geometry of the fault, and the shortening rate of the thrust fault.

3.2. Surface Exposure Dating

We used ^{10}Be exposure dating to determine the age of terrace formation in the hanging wall of the Danghe Nan Shan frontal thrust. For dating depositional landforms such as river terraces or alluvial fans with cosmogenic nuclides, there exist two main approaches. The first approach involves the analysis of several individual cobbles or boulders from a single geomorphic surface (e.g., Brown et al., 1998; van der Woerd

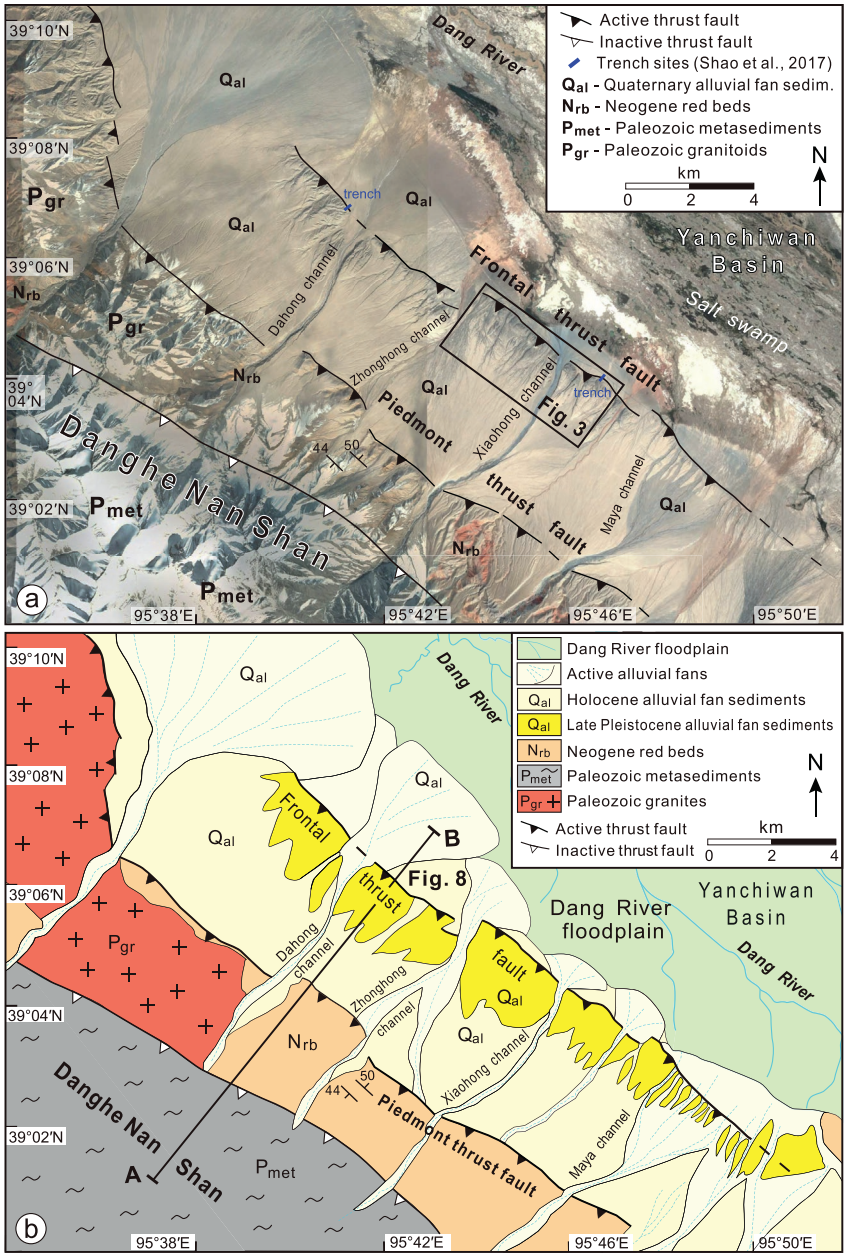

Figure 2. (a) Satellite image (Google Earth) showing the major thrust faults in the northeastern piedmont of the Danghe Nan Shan. Two active thrust faults cut alluvial fan sediments and form fault scarps. Two trench sites at the Danghe Nan Shan frontal thrust fault are from Shao et al. (2017). Black rectangle marks the area depicted in Figure 3. (b) Geological map of the region shown in (a) based on Gansu Geological Bureau (1975), Meyer et al. (1998), and Shao (2010).

et al., 1998). Ideally, the exposure ages obtained from the sampled cobbles or boulders fall in a relatively narrow range, with no or only a few ages being significantly older (e.g., Chevalier et al., 2016; Hetzel et al., 2019; Ritz et al., 2003; van der Woerd et al., 1998). These older ages can be interpreted as outliers, which overestimate the age of the surface due to the presence of a pre-depositional or inherited nuclide component. The second approach uses amalgamated samples (each consisting of at least 30 pebbles) from the geomorphic surface to be dated (Anderson et al., 1996; Repka et al., 1997). In this case, the inherited nuclide component can be constrained by fitting an exponential curve to the age-depth data. Alternatively, the inheritance can be determined with amalgamated samples from active streams, assuming that the nuclide concentration of the stream sediments is similar to the inheritance of the material deposited during terrace

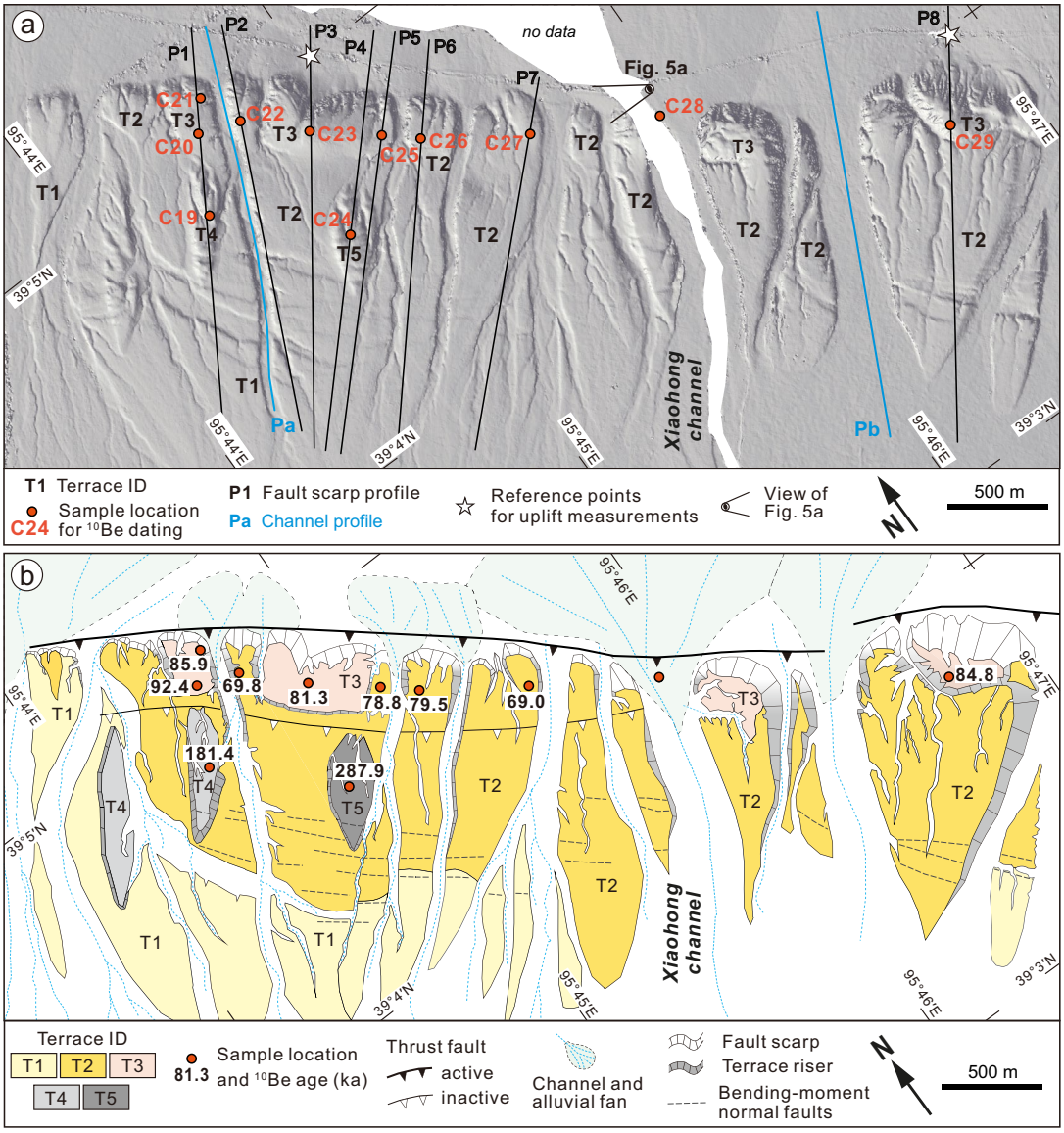

Figure 3. (a) High-resolution (1.5 m cell size) digital elevation model at the Xiaohong channel located at the Danghe Nan Shan frontal fault derived from Worldview two satellite images. The position of the samples taken for ^{10}Be exposure dating are shown by red circles. Topographic profiles are indicated by solid lines. The star marks the reference point used for determining the uplift from the topographic profiles (Figure 4). See text for further explanation. (b) Geomorphologic map showing the five terrace levels in the hanging wall of the Danghe Nan Shan frontal thrust and the ^{10}Be exposure ages.

or alluvial fan formation. Studies that applied the two different approaches to date depositional surfaces in the arid regions of Central Asia indicate that both methodologies provide consistent and reasonable ages for landforms up to a few hundred thousand years in age (e.g., Cording et al., 2014; Hetzel et al., 2019, 2002; Huang et al., 2014; Saint-Carlier et al., 2016; Wang et al., 2020; Yang et al., 2018).

In this study, we used the amalgamation approach because cobbles or boulders do not occur on the terraces at the Danghe Nan Shan frontal thrust. All sampled terrace surfaces are well preserved, with no evidence for modification by humans or animals. We chose flat and pristine parts of the fluvial terraces as sampling sites, carefully avoiding any rills formed by flowing water. In total, we collected 10 samples from four different terrace levels (Figures 3a, 5a). Each sample was collected from the top of a terrace surface and consisted of 50–100 quartz clasts with a size of 2–4 cm. The quartz pebbles selected for each sample were partly imbedded in the terrace sediments and were sampled over areas of ~30 to ~300 m^2 (Figures 5b–5d), with the size depending on terrace width and the extent of the most pristine terrace parts. To determine the

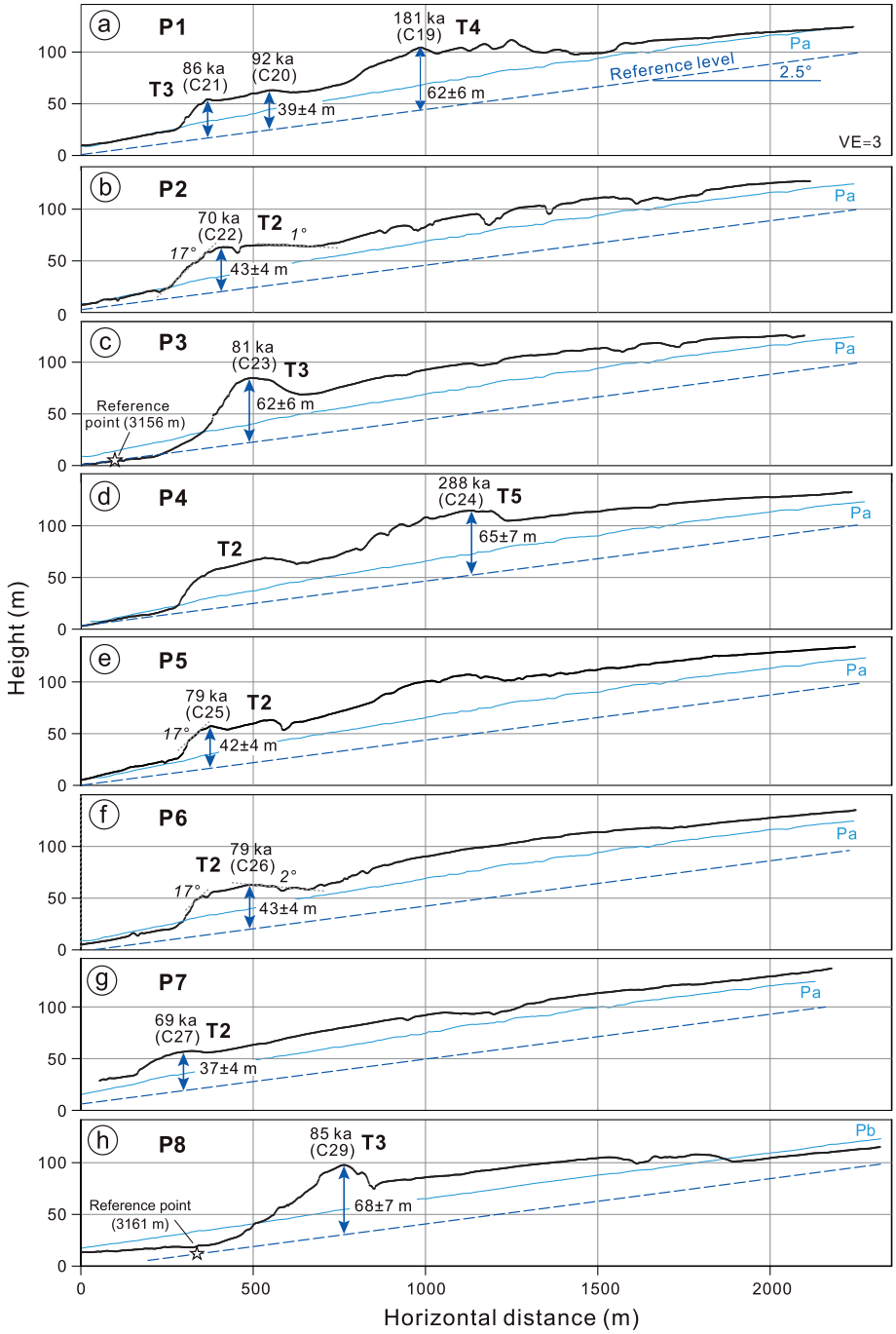

Figure 4. Scarp profiles (P1–P8) extending along the different river terraces and through the sampling sites. The double-headed blue arrows indicate the amount of uplift on each profile. The reference channel profile (blue dashed line) starts from the reference site marked by star with an elevation of 3156 m and has a slope of 2.5° (similar to stream profile Pa). On the easternmost profile P8, we increased the elevation of the reference level by 5–3651 m, based on the gradient of the Dang River of 1%. The profile of the nearby channel Pb is shown as well.

inheritance, an additional amalgamated quartz-clast sample was taken from the active Xiaohong stream channel (Figure 3a).

Sample preparation was done at the Institute of Geology and Paleontology, University of Muenster. After crushing, sieving, and washing, the 250–500 μm grain-size fraction was split into a magnetic and non-magnetic fraction using a Frantz magnetic separator. The non-magnetic fraction was etched once in 6M HCl at

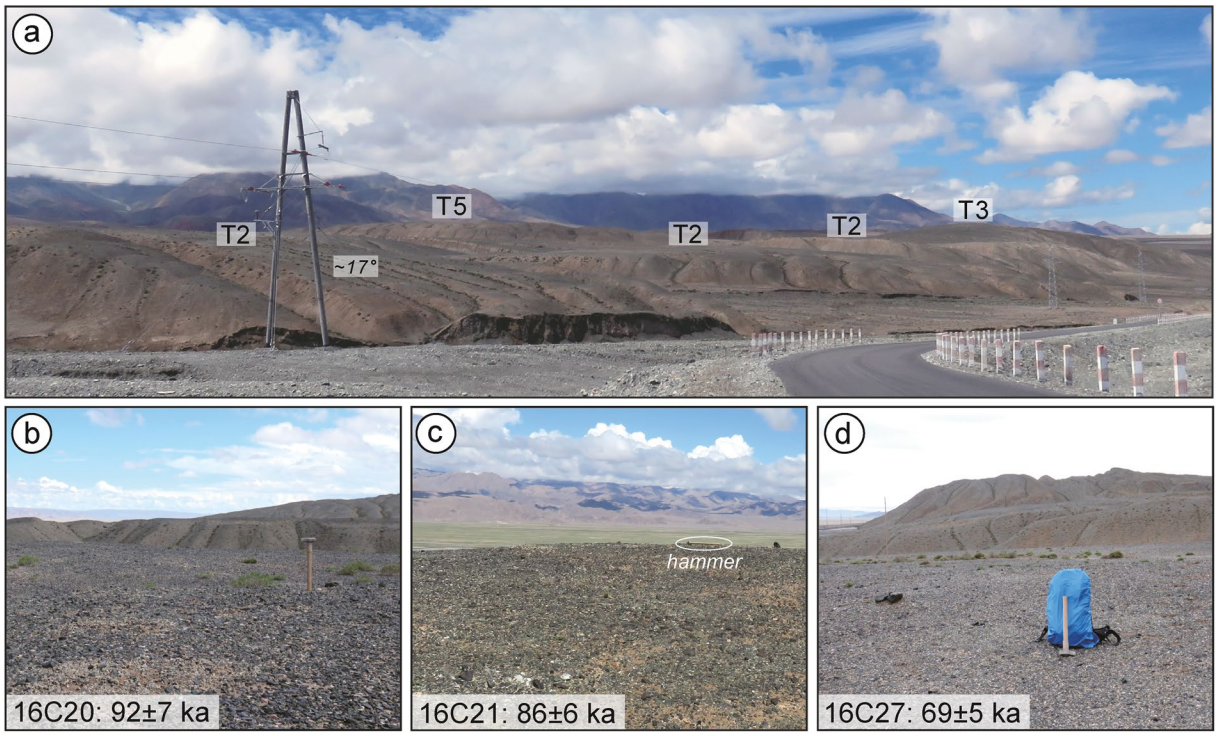

Figure 5. Field photographs showing the fluvial terraces and representative sampling sites. (a) Oblique view of thrust-fault scarp with terraces T2, T3, and T5 in the hanging wall. In the foreground on the left, the NE-dipping portion of the folded terrace T2 can be seen. Photo was taken from 39.0734°N, 95.7634°E (position is indicated in Figure 3a). View direction is to the WNW. (b) Sampling site of amalgamated quartz sample 16C20 on terrace T3 (39.0843°N, 95.7430°E). The quartz clasts were collected from an area of 30 × 5 m. View is to the SE. Hammer for scale is 53 cm long. (c) Sampling site of 16C21 on terrace T3 (39.0855°N, 95.7446°E). Quartz clasts were collected from an area of 6 × 5 m. View is to the (e). Note hammer for scale. (d) Site of quartz-clast sample 16C27 (39.0752°N, 95.7582°E), which was taken on terrace T2 from an area of 10 × 30 m. View is to the SE. Note hammer for scale.

80°C followed by four etching steps in dilute HF/HNO_3 in an ultrasonic bath heated to 80°C. For Be extraction, 20–25 g of quartz from each sample was dissolved in 40% HF after addition of 0.3 mg of Be carrier. After complete dissolution, all samples were converted into chloride form using 6M HCl. Beryllium was separated by ion exchange column chemistry and precipitated as $Be(OH)_2$ at pH 8–9. Following the transformation to BeO at 1000 °C, targets were prepared by mixing of the BeO with Nb powder. All samples were analyzed at the Center for Accelerator Mass Spectrometry at the University of Cologne, Germany (Cologne AMS; Dewald et al., 2013).

The ^{10}Be exposure ages were calculated with version 3 of the CRONUS-Earth ^{10}Be – ^{26}Al online calculator (http://hess.ess.washington.edu; Balco et al., 2008) using the time-dependent scaling model of Lifton et al. (2014), which is referred to as LSDn in the online calculator and based on the calibration dataset of Borchers et al. (2016). All ages were calculated assuming a rock density of 2.65 g cm^{-3} and zero erosion. To account for an inherited nuclide component in the terrace samples, we subtracted a ^{10}Be concentration of 20 ± 10 × 10^4 at/g, which is based on the sample from the active channel (16C28) and a conservative uncertainty of 50% (Table 1). Note that this correction is rather small and reduced the measured ^{10}Be concentration of all samples by ≤6.5%. The mass of the quartz samples and the Be carrier, as well as the $^{10}Be/^{9}Be$ ratios of the samples and two blanks are given in Table S1.

4. Results

4.1. Terrace Mapping

In the study area, three main terrace levels (T1–T3) have developed in the hanging wall of the thrust fault (Figure 3). The terraces are dissected by intermittent channels, forming spindle-shaped patches that are truncated by the fault scarp. The lowest terrace T1 merges gradually with the NE-facing bajada surface

Tectonics

10.1029/2020TC006584

Table 1
Information on ^{10}Be Exposure Dating of Samples From Fluvial Terraces in the Hanging Wall of the Danghe Nan Shan Frontal Thrust

Terrace number	Sample number	Latitude [°N]	Longitude [°E]	Sample elevation [m]	Sample thickness (cm)	Topographic shielding	^{10}Be concentration[a] (10^4 at g^{-1})	^{10}Be exposure age[b] [ka]	Internal uncertainty [ka]	External uncertainty [ka]	Amount of uplift [m]	Uplift rate[c] [m ka^{-1}]
T2	16C22	39.0841	95.7459	3240	2	1.00	290.4 ± 13.8	69.8	±3.4	±5.4	43 ± 4	0.62 ± 0.07
T2	16C25	39.0788	95.7511	3242	2	1.00	327.2 ± 14.6	78.8	±3.6	±6.0	42 ± 4	0.53 ± 0.06
T2	16C26	39.0781	95.7529	3235	2	1.00	328.6 ± 14.7	79.5	±3.6	±6.0	43 ± 4	0.54 ± 0.06
T2	16C27	39.0752	95.7582	3231	2	1.00	285.6 ± 13.9	69.0	±3.4	±5.4	37 ± 4	0.54 ± 0.07
T3	16C20	39.0843	95.7430	3240	2	1.00	384.8 ± 16.0	92.4	±3.9	±6.8	39 ± 4	0.42 ± 0.05
T3	16C21	39.0855	95.7446	3231	2	1.00	354.6 ± 15.2	85.9	±3.8	±6.4	39 ± 4	0.45 ± 0.06
T3	16C23	39.0812	95.7477	3258	2	1.00	340.8 ± 15.2	81.3	±3.7	±6.1	62 ± 6	0.76 ± 0.09
T3	16C29	39.0637	95.7778	3272	2	1.00	358.8 ± 15.6	84.8	±3.8	±6.4	68 ± 7	0.80 ± 0.10
T4	16C19	39.0811	95.7408	3280	2	1.00	790.0 ± 27.3	181.4	±6.6	±13.0	62 ± 6	*0.34 ± 0.04*
T5	16C24	39.0759	95.7454	3289	2	1.00	1256.2 ± 41.3	287.9	±10.2	±20.9	65 ± 7	*0.23 ± 0.03*
River	16C28	39.07234	95.7639	3228	–	–	19.8 ± 0.7	–	–	–	–	–

[a]^{10}Be concentrations were measured at the Cologne AMS, Germany (Dewald et al., 2013) and are normalized to the standards KN01-6-2 and KN01-5-3 with nominal ^{10}Be/^{9}Be ratios of 5.349×10^{-13} and 6.320×10^{-12}, respectively. We also analyzed two aliquots of the quartz reference material CoQtz-N with a ^{10}Be concentration of $2.53 \pm 0.09 \times 10^6$ at/g (Binnie et al., 2019), for which we obtained ^{10}Be concentrations of 2.40 ± 0.09 and $2.61 \pm 0.09 \times 10^6$ at/g, respectively. The uncertainties of the ^{10}Be concentrations (1σ) include the analytical uncertainty and the error of the blank correction. The analytical uncertainty includes the error based on the counting statistics, the scatter of repeated measurements of the same sample, and the uncertainty of the standard normalization. Note that the ^{10}Be concentrations reported for the terrace samples were corrected for an inherited ^{10}Be component of $20 \pm 10 \times 10^4$ at/g, based on the ^{10}Be concentration of the amalgamated sample 16C28 from an active stream channel. [b]^{10}Be exposure ages were calculated with the CRONUS-Earth ^{10}Be–^{26}Al online calculators (http://hess.ess.washington.edu/, version 3), using the time-dependent scaling model of Lifton et al. (2014), referred to as LSDn in the online calculator. All ages were calculated assuming a rock density of 2.65 g cm^{-3} and zero erosion. [c]Uplift rates were calculated by dividing the amount of uplift (Figure 4) by the ^{10}Be exposure ages. Note that the uplift rates derived from terraces T4 and T5 integrate over a time period, during which the frontal thrust fault propagated to its current position. These rates are therefore shown in italics (see text for details).

of the Danghe Nan Shan (Figures 2 and 3), which dips at an angle of ~2.5° (Figure S1). Compared to T1, terrace T2 is more extensive and has been clearly deformed by an asymmetric, NE-vergent anticline that trends parallel to the fault scarp. At the steeper forelimb of the fold, terrace T2 dips at an angle of ~17° to the NE (Figure 4, profiles P2, P5, and P6; Figure 5a), whereas in the backlimb, it dips 1–2° to the SW (Figure 4, profiles P2 and P6). On terrace T1 and the southwestern part of terrace T2, minor NW-SE striking faults are observed, which are presumably bending-moment normal faults (e.g., Li et al., 2018). Terrace T3 is only preserved in dome-shaped terrace patches along the crest of the anticline. Folded Quaternary sediments below terrace T2 are exposed in a cliff east of the Xiaohong stream channel, where bedding planes dip ~29° NE in the forelimb and ~12° SW in the backlimb. Taken together, the observations above indicate that the spatial distribution of T1–T3 reflects the progressive growth of the asymmetric anticline with concomitant incision of channels, sediment transport, and deposition of alluvial fans in front of the scarp.

An older thrust fault striking parallel to the active one is located southwest of terrace T3 (Figure 3b). In the hanging wall of this fault occur the highest, and presumably oldest terrace patches, T4 and T5, on top of spearhead-shaped hills. These terrace remnants appear to have escaped erosion because the hanging wall was uplifted when the thrust fault was still active. However, as terrace T2 in the vicinity of this fault does not appear to be deformed, the fault is likely not active anymore. It may have been abandoned when deformation propagated toward the foreland and the currently active thrust fault formed ~500 m farther to the NE (Figure 3b).

4.2. Terrace Uplift at Fold Hinge

To determine the uplift of the fluvial terraces by faulting and folding, we constructed eight topographic profiles, P1–P8, across the fault scarp and the different terraces (Figures 3 and 4). Note that the profiles extend only a few hundred meters to the NE of the fault because the alluvial fan sediments deposited in front of the fault scarp soon transition into the subhorizontal floodplain of the Dang River (Figure 2; see Figure S1). Due to the partial coverage of the footwall of the active fault by alluvial fan sediments, it is necessary to account for the deposition of these sediments when measuring the amount of uplift. We achieved this in the following way. First, we identified the lowest point along the base of the fault scarp, which occurs between two alluvial fans (Figure 3a, reference point on profile P3). This point does not receive sediment from active channels, and therefore, sediment accumulation during fold growth is considered to be negligible here. Second, we assume that along strike of the fault, the topography at the front of the current scarp had the same elevation as the reference point (i.e., 3156 m) before activation of the frontal thrust. In other words, we neglect a potential curvature of the original fan surface because the distance between profiles P1 and P7 is <2 km, and the resulting height differences would probably be small. For profile P8, which is located a few kilometers farther southeast, we considered the local gradient of the Dang River of 1% and used a reference point at an elevation of 3161 m (i.e., 5 m higher than the one for P1–P7). Third, we used the current gradient of ~2.5° of two large channels as a proxy for the dip of the undisturbed fan surface before faulting started (i.e., profiles Pa and Pb in Figure 3a) because the slope of the original fan surface is not preserved. A value of ~2.5° is also supported by the slope of the modern fan surfaces (see Figure S1), although this does not rule out that the original fan might have had a slightly different surface slope than the modern fans. The reference level resulting from using a gradient of 2.5° for all profiles is shown as dashed blue line in Figure 4. We determined the vertical displacement of the terraces T2 and T3 at the fold hinge as the vertical distance between the reference level and these terrace levels along strike of the fault. For terrace T2, we obtain four consistent uplift values between 37 ± 4 m and 43 ± 4 m (Figure 4). The three values for T3 are more variable, ranging from 39 ± 4 m to 68 ± 7 m, while those for T4 and T5 are 62 ± 6 m and 65 ± 7 m, respectively (Table 1).

4.3. Terrace Ages and Uplift Rates

The results from ^{10}Be surface exposure dating are shown in Figure 3 and Table 1. The four samples from the different patches of terrace T2 (16C22, –C25, –C26, –C27) yielded ^{10}Be exposure ages ranging from 69.0 ± 5.4 ka to 79.5 ± 6.0 ka. The samples from terrace T3 have ^{10}Be ages between 81.3 ± 6.1 ka and 92.4 ± 6.8 ka; samples from T4 and T5 yielded much older ^{10}Be exposure ages of 181 ± 13 ka and 288 ± 21 ka,

respectively. As all samples from terraces T2 and T3 are located on the crest of the actively growing anticline, we combined the ^{10}Be exposure ages with the respective uplift values to calculate uplift rates along strike of the thrust fault. The resulting uplift rates range from 0.42 ± 0.05 to 0.80 ± 0.10 mm/year (Table 1), with an average value of 0.6 ± 0.2 mm/year. The uncertainties of these uplift rates were determined by Gaussian error propagation assuming that the errors of the exposure ages and the uplift values have a normal distribution.

As explained in Section 4.1, the terraces T4 and T5 are located in the hanging wall of a thrust fault that is presumably not active anymore. This interpretation would explain why the uplift rates calculated for these terraces are relatively low (i.e., ~0.3 and ~0.2 mm/year, respectively). Both rates integrate over a long time period during which the frontal thrust fault propagated to its current position. In any case, the remarkably high ^{10}Be exposure ages obtained for the terraces T4 and T5 indicate that fluvial terraces along tectonically mountain ranges can be preserved for up to ~300 ka in the arid environment of northern Tibet. Comparably high (and even higher) exposure ages have been obtained in other areas in Central Asia (e.g., Cording et al., 2014; Huang et al., 2014; Yang et al., 2018).

4.4. Shortening Rate from Fold Shape, Fault Geometry, and Area Balancing

The fold in the hanging wall of the active Danghe Nan Shan thrust fault has a relatively steep forelimb, a nearly planar hinge zone, and a shallow-dipping backlimb. Its geometry is most clearly visible on profiles P2, P4, and P6 from the shape of the deformed terrace T2 (Figure 3). The geometry of the ~500-m-wide asymmetric anticline is similar to folded river terraces that occur at a larger scale along the mountain front of the Qilian Shan, and suggests the presence of a listric fault, with a steeper segment near the surface and a shallower segment at greater depth (cf. Hu et al., 2015; Liu et al., 2019; Wang et al., 2020; Zhong et al., 2020). Note that the bending-moment normal faults (Figure 3) occur in the southwestern part of terrace T2 and do not affect the anticline related to the frontal thrust, on which we base the subsequent analysis.

In the following, we apply the geometric model and nomenclature of Hu et al. (2015) to derive the subsurface geometry of the thrust fault from the shape of the asymmetric fold on profiles P2 and P6. First, we rotated these profiles, on which the shape of the folded terrace T2 is most clearly seen, by 2.5° so that the reference level becomes horizontal (Figure 6). Note that Figure 6 shows the rotated topographic profiles with a horizontal reference level, but this minor rotation is ignored when deriving the vertical and horizontal distances, as well as fault dip angles for the following analysis (cf. Hu et al., 2015; Zhong et al., 2020). In particular, the dip angles represent the natural fault dips (i.e., they are not tilted back). The width of the fold on the two profiles is defined by the horizontal extent of the forelimb (d_1), the axial top (d_2), and the backlimb (d_3), and is 500 m on P2 and 445 m on P6, respectively. At the axial top of the fold, the uplift of terrace T2 above the reference level, h_1, is 43 ± 4 m, whereas the uplift at the end of the backlimb, h_2, amounts to 33 ± 3 and 34 ± 3 m, respectively (Figure 6). Note that we do not use the elevation of the channel Pa for measuring h_1 and h_2, because this would neglect the sediments deposited at the base of the scarp and farther upstream after faulting began. Using the assumption of a uniform slip along the fault plane (cf. Hu et al., 2015; Thompson et al., 2002), the change in fault dip between the steep and shallow fault segments can be determined from the values of h_1 and h_2 using the following equation:

$$h_1 / \sin(\alpha_1) = h_2 / \sin(\alpha_2) \quad (1)$$

Based on outcrop observations of Shao et al. (2010), we use a value of 40° for α_1, to which we assign an uncertainty of ±10°, and obtain values for α_2 of 30 ± 6° and 31 ± 6° from profiles P2 and P6, respectively (Figure 6). The depth of the inflection points at the upper and lower end of the listric fault segment (points A and B in Figure 6) can be calculated with the following equations (Hu et al., 2015):

$$H_1 = \left(\frac{d_1}{2} + d_2\right) \times \sin(\alpha_1) \times \cos(\alpha_1) \quad (2)$$

$$H_2 = \left[\left(\frac{d_1}{2} + d_2\right) \times \sin\alpha_1 + \frac{d_3}{\sin(\alpha_1 - \alpha_2)} \times (\cos\alpha_2 - \cos\alpha_1)\right] \times \cos\alpha_2 \quad (3)$$

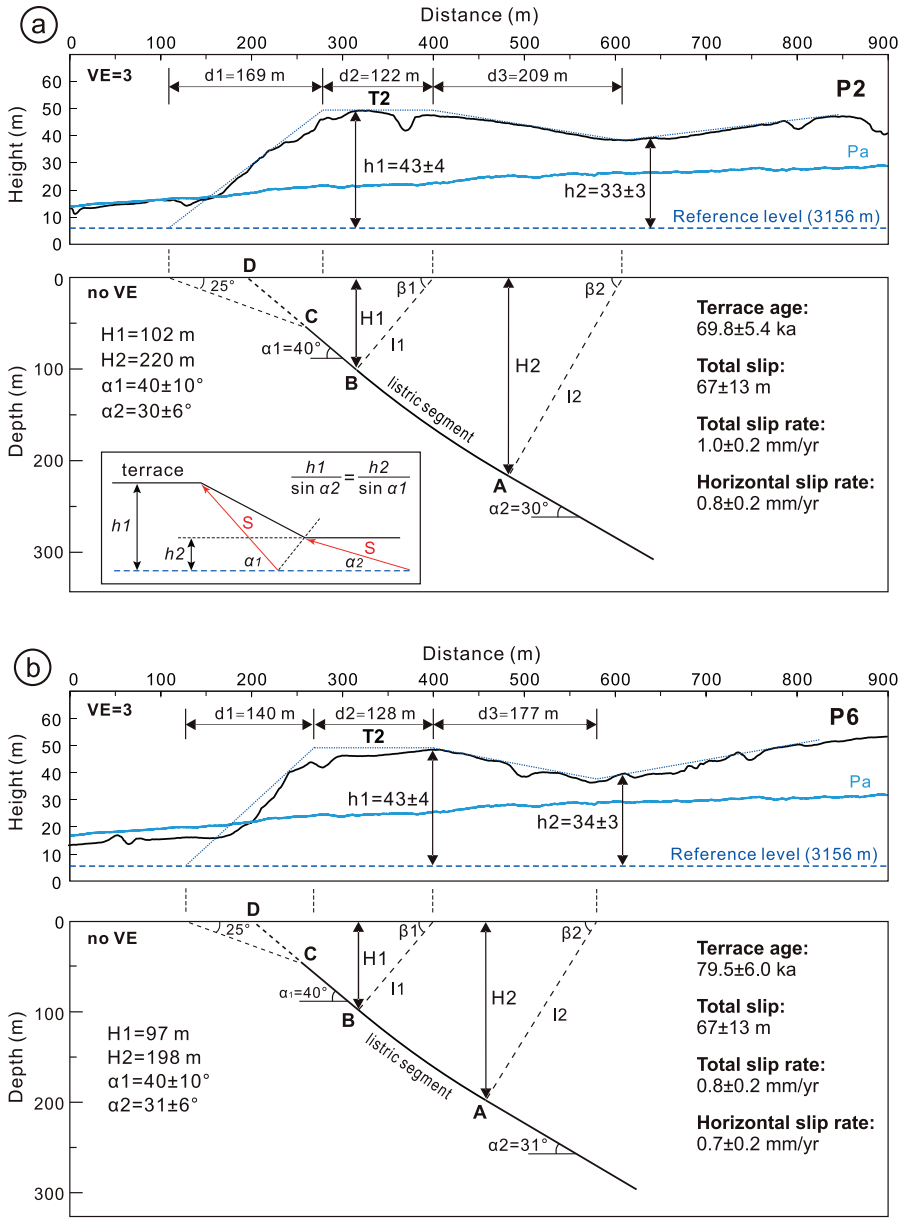

Figure 6. Topographic profiles P2 (a) and P6 (b) across the folded terrace T2 and modeled subsurface geometry of the thrust fault at depth. Both profiles were rotated by 2.5° so that the reference level is horizontal. Parameters d1, d2, and d3 are the horizontal length of the forelimb, the axial top, and the backlimb of the fold, whereas h1 and h2 are the terrace heights above the reference level at the axial top and just upstream of the backlimb. Points A and B delimit the listric fault segment, whereas H1 and H2 refer to the depth range of this segment. α1 and α2 are the dip angles of the planar fault segments above and below the listric fault segment. The planar fault dips 40° between B and C but has a shallower dip of ~25° close to the surface as revealed by paleoseismic trenches (Shao et al., 2017; for trench location see Figure 2). Inset shows the relation between terrace heights, fault slip S, and fault dip angles (cf. Hu et al., 2015).

The resulting depths of points A and B are ~100 and ~200 m, respectively; the exact values are given in Figure 6.

The total slip on the fault S since the formation of terrace T2 can be determined with the following equation (cf. Hu et al., 2015)

$$S = \frac{h_1 - h_2}{\sin \alpha_1 - \sin \alpha_2} \tag{4}$$

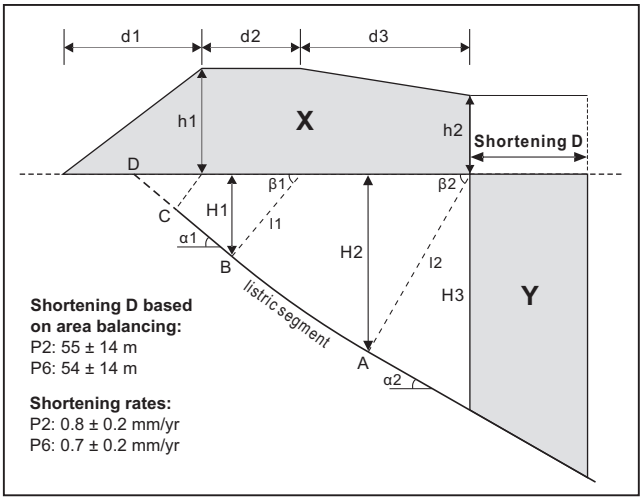

Figure 7. Sketch illustrating the approach to quantify the amount of horizontal shortening D from the cross-sectional area of the fold (X) and the geometry of the thrust fault, which is based on Hu et al. (2015). See text for further explanation.

and is 67 ± 13 m. For estimating the uncertainty of S, we used the upper and lower error limit of α_1 (i.e., 50° and 30°) to calculate α_2 values of 36° and 23° and the error bounds of S, respectively. Regarding the error of the height difference ($h_1 - h_2$), we assumed that it is negligible, because this value can be directly determined from the high-resolution DEM (i.e., it is independent from the position of the reference level). When combined with the ^{10}Be exposure ages for terrace T2 on profiles P2 and P6 (i.e., 69.8 ± 5.4 ka and 79.5 ± 6.0 ka), the total slip value of 67 ± 13 m yields fault slip rates of 1.0 ± 0.2 mm/year and 0.8 ± 0.2 mm/year, respectively. The horizontal shortening rates above the steep fault segment (i.e., $\alpha_1 = 40°$) are then 0.7 ± 0.2 and 0.6 ± 0.2 mm/year (Figure 6). The uncertainties on these rates were again obtained by Gaussian error propagation.

An alternative approach to determine the horizontal shortening rate is to assume that the cross-sectional area during folding and deformation has been preserved. Hence, the area of the anticline, X, and the area above the shallow part of the thrust fault, Y, should be the same (Figure 7). The areas X and Y can be quantified with the following two equations (cf. Hu et al., 2015):

$$X = \frac{h_1 d_1}{2} + h_1 d_2 + h_2 d_3 + \frac{(h_1 - h_2) d_3}{2} \quad (5)$$

$$Y = D^2 \times \frac{\tan \alpha_2}{2} + H_3 \times D \quad (6)$$

All values required to calculate the fold area X are given in Figure 6. Solving Equation 6 for the amount of horizontal shortening D and assigning a conservative uncertainty of 25% to D yield values of 55 ± 14 m and 54 ± 14 m (Figure 7). Combining these shortening values with the ^{10}Be ages for terrace T2 on profiles P2 and P6, we obtain shortening rates of 0.8 ± 0.2 and 0.7 ± 0.2 mm/year (with uncertainties obtained by Gaussian error propagation).

5. Discussion

5.1. Slip Rate of the Danghe Nan Shan Frontal Thrust fault

By evaluating high-resolution topographic profiles across the Danghe Nan Shan frontal thrust and applying ^{10}Be exposure dating to amalgamated quartz-clast samples from deformed river terraces, we obtained a mean uplift rate of 0.6 ± 0.2 mm/year in the hinge region of the 500-m-wide anticline, which grows in the hanging wall of this active fault. As the ^{10}Be exposure ages were calculated with the assumptions of no erosion and no cover (e.g., by snow or loess), they are, strictly speaking, minimum ages. Therefore, the uplift rates calculated from the different samples should be regarded as maximum rates (Table 1). Another factor affecting our uplift rates is the amount of sediment that was deposited at the toe of the fault scarp and in the channels farther upstream. We corrected for the presence of these sediments by using a reference level that extends from the reference point on profile P3 upstream with a dip of 2.5° (Figure 4). The value of 2.5° is the average gradient of two channels located in the western and eastern part of the study area, respectively (profiles Pa and Pb in Figure 3a). As the distance from the base of the scarp to the terrace samples at the fold hinge is rather small (<400 m for terraces T2 and T3), we assigned an uncertainty of ±10% to the uplift values (Figure 4). If we overestimated the sediment thickness with the approach outlined above, the uplift values and the uplift rates reported in Table 1 would be too high. Using the uplift rates determined on profiles P2 and P6 and a fault dip of 40° (Shao et al., 2010), we determined shortening rates of 0.7 ± 0.2 and 0.6 ± 0.2 mm/year since the formation of terrace T2 (Figure 6). Our preferred shortening rates of 0.8 ± 0.2 and 0.7 ± 0.2 mm/year, which are consistent with these values, were obtained with the assumption that the cross-sectional area of the fault-related fold did not change during faulting (Figure 7). Assuming an average fault dip of ~30° (cf. Figure 8), the total slip rate of the Danghe Nan Shan frontal thrust can be estimated to be about 0.9 mm/year.

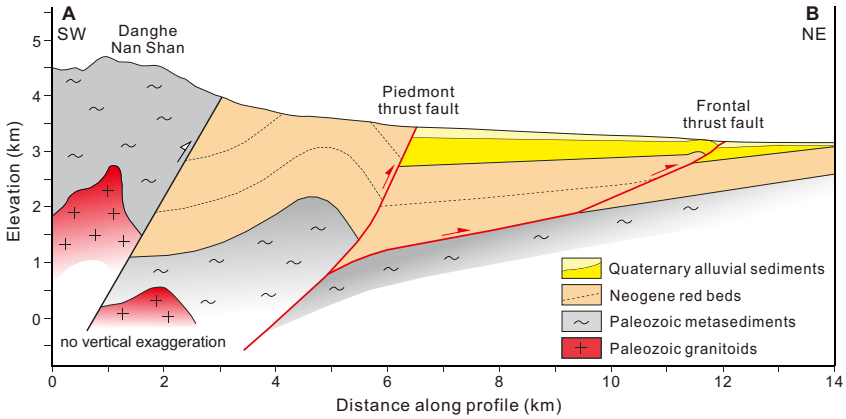

Figure 8. Geological profile across the Danghe Nan Shan based on this study, Meyer et al. (1998) and Shao (2010). For location see Figure 2.

Our uplift and shortening rates are much lower than those determined for the active thrust fault in the northwestern part of the Danghe Nan Shan, which defines the southern margin of the Subei Basin (Figure 1). Here, a vertical slip rate of 4.1 ± 0.5 mm/year and a shortening rate of 5.5 ± 1.5 mm/year were derived by van der Woerd et al. (2001) based on radiocarbon dating of deformed and tectonically offset river terraces of Holocene age. The difference in the shortening rate along-strike of the Danghe Nan Shan can be explained by the presence of two other active faults. First, the left-lateral Yema River–Daxue Shan fault (YRDS in Figure 1) extends from the eastern margin of the Subei Basin toward the ENE and causes crustal material south of the fault to move away from the Danghe Nan Shan and our study area. The left-lateral kinematics of this fault thus causes differential crustal shortening, with a higher rate in the west (i.e., south of Subei) and a lower rate farther to the southeast along the Danghe Nan Shan. The second fault is the steep Danghe Nan Shan piedmont thrust fault (Figure 2), which accommodates additional NE-SW shortening across the Danghe Nan Shan as discussed in the following section.

5.2. Crustal Shortening Across the Danghe Nan Shan and Comparison with GPS Data

Paleoseismic investigations revealed the presence of a young fault scarp with a height of 0.8 ± 0.2 m, clearly demonstrating that the Danghe Nan Shan frontal thrust fault is active and capable of producing major earthquakes (Shao et al., 2017). With respect to the entire shortening across the central Danghe Nan Shan, our shortening rates of ~0.7 and ~0.8 mm/year represent minimum values because additional shortening is caused by the Danghe Nan Shan piedmont thrust fault (Figure 8). As we were unable to reach the respective fault scarp during our field investigations, the shortening rate of the piedmont thrust remains unknown. If, for simplicity, we assume that that piedmont thrust fault has the same shortening rate as the frontal thrust, the total shortening rate accommodated by the two faults would be 1.5 mm/year. However, the observation that the piedmont fault dips steeply (>70°) (Shao, 2010) suggests that it causes less shortening than the frontal thrust. Hence, we propose a tentative shortening estimate across the entire Danghe Nan Shan of 1.0–1.5 mm/year. With respect to the different geomorphological expressions of the two faults (Figure 2), the piedmont thrust fault appears more pronounced than the frontal thrust fault because its steep dip results in a higher vertical slip component compared to the shallower-dipping frontal thrust. Also, the piedmont thrust is located near the mountain front where rivers have steeper gradients, whereas the frontal thrust is located at a more distal position, where alluvial-fan sediments locally buried its scarp (e.g., profile PA1, Figure S1). Together with its lower vertical slip component, this explains why the frontal thrust may appear less distinct than the piedmont thrust, although the former contributes a larger percentage to the total shortening rate across the Danghe Nan Shan.

We now compare the millennial shortening rate across the Danghe Nan Shan with a shortening rate that we derive from GPS data, which span a period of 25 years (Gan et al., 2007; Wang & Shen, 2020) (Figure 1). To do so, we calculated the velocity component parallel to the direction N35°E (i.e., perpendicular to the strike of the active thrust faults) from the total GPS velocity vectors (light blue-headed arrows in Figure 1).

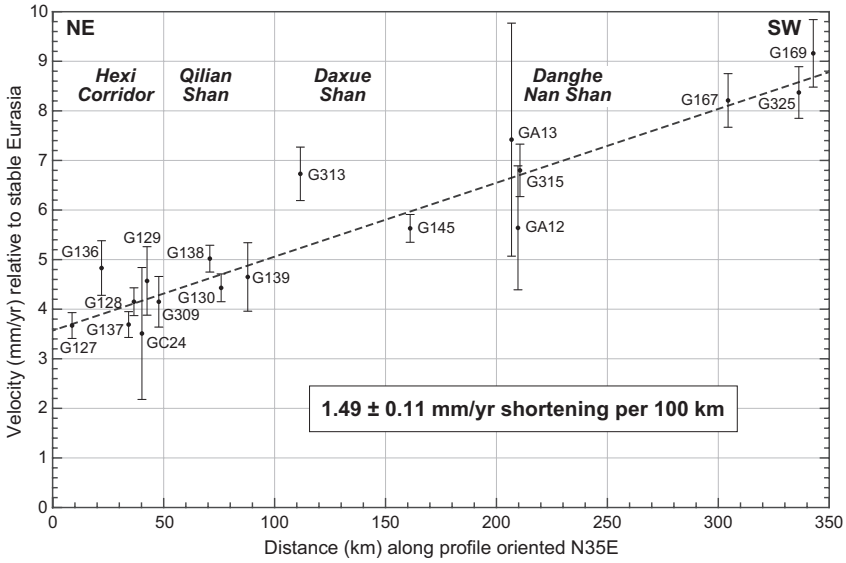

Figure 9. GPS velocities for 18 GPS stations projected onto a 350-km-long profile across NE Tibet (for location see Figure 1). The GPS data indicate ~1.5 mm/year of elastic strain accumulation per 100 km in the direction N35°E, which is equivalent to a total shortening rate of ~5.2 mm/year that is caused by thrust faulting in the Danghe Nan Shan (this study), the Daxue Shan, and the Qilian Shan (Hetzel et al., 2019; Liu et al. 2017a, 2019; Wang et al. 2020; Yang et al. 2018).

Plotting these velocity components along a 350-km-long profile (extending from the eastern Qaidam basin to the Hexi Corridor) and least-square fitting of a straight line through the data (cf. York, 1966), yields a shortening rate of 1.49 ± 0.11 mm/year per 100 km (Figure 9). To compare this GPS-based rate of elastic strain accumulation with our millennial shortening rate of 1.0–1.5 mm/year, we need to know the width of the zone over which elastic deformation is transformed into permanent strain by slip on the two thrust faults. Field, modeling, and geodetic studies indicate that the zone affected by coseismic deformation is 60–100 km wide for thrust faults (e.g., Ader et al., 2012; Ellis & Densmore, 2006; Hampel & Hetzel, 2015; Marshall et al., 2013; Stein et al., 1988). If elastic strain accumulating during the interseismic period is released over a width of 60–100 km during repeated earthquakes, 0.9–1.5 mm/year of long-term shortening would be expected across the Danghe Nan Shan based on the GPS data. Hence, the shortening rates on millennial and decadal timescales are in remarkably good agreement. A similarly good accordance between shortening rates on different timescales was obtained for the Qilian Shan frontal thrust (Hetzel et al., 2019).

Finally, we note that the total GPS velocity vectors for stations east and south of Subei (shown with dark blue arrow heads in Figure 1) are oriented roughly perpendicular to the strike of the Danghe Nan Shan. Hence, the GPS data do not provide any evidence for left-lateral strike-slip faulting along the Danghe Nan Shan and argue against previous interpretations of sinistral strike-slip motion on steep faults in the interior of the Danghe Nan Shan (e.g. Meyer et al., 1998). We note that the only exception [i.e., the obliquely oriented velocity vector of GPS station GA13 from Gan et al. (2007)] would indicate a dextral rather than a sinistral slip component.

5.3. Strain Distribution in Northern Tibet near the Altyn Tagh fault

In this section we summarize the results of slip-rate studies that constrain the rates of thrusting and strike-slip faulting in the Qilian Shan and the interior of Tibet (i.e., excluding the Altyn Tagh fault) on timescales of 10^4–10^5 years. Then, we sum up the rates of horizontal shortening determined for the different faults to calculate the total shortening rate and compare this value with the rate of elastic strain accumulation recorded by GPS data (Figure 9). Along the western Qilian Shan frontal thrust, the rate of shortening has been determined at five sites over timescales of 50–200 ka with ^{10}Be exposure dating of deformed river terraces

(Hetzel et al., 2019; Liu et al., 2017a, 2019; Wang et al., 2020; Yang et al., 2018). The shortening rates are between ~1.1 and ~2.0 mm/year, with the weighted mean value of all rates being 1.6 ± 0.2 mm/year.

At the boundary fault of the Daxue Shan, slip rate studies on millennial timescales have not yet been performed. Therefore, we choose a different approach and estimate the shortening rate across the Daxue Shan from the slip rate determined for the Yema River–Daxue Shan (YRDS) strike-slip fault. Near the eastern end of the fault (site L1c in Figure 1), a left-lateral slip rate of 2.82 ± 0.20 mm/year has been derived from a tectonic offset of 16 ± 1 m and a ^{14}C age of 5670 ± 35 years (Luo et al., 2015). However, the small and symmetric error of this radiocarbon age indicates that it has not been calibrated. Calibration of this ^{14}C age using the IntCal20 calibration curve (CALIB software, version 8.2; Reimer et al., 2020) yields a calibrated age range of 6555–6321 cal. years BP (2σ) with a median age of 6448 years. Using the mean value of this range and a symmetrical error results in an age of 6440 ± 120 cal. years BP (when rounding to the nearest 10 years). Calculating the slip rate of the YRDS fault with this revised age gives a value of 2.5 ± 0.2 mm/year at site L1c. This slip rate is consistent with the slip rates determined by OSL dating at sites L1a and L1b of the YRDS strike-slip fault, which are 2.50 ± 0.36 mm/year and 2.0 ± 0.24 mm/year, respectively (Luo et al., 2015). Assuming that the entire strike-slip motion at site L1c of the YRDS strike-slip fault is transferred to the range-bounding thrust fault of the Daxue Shan, we can calculate the shortening rate of the latter. Taking into account the 30° difference between the strike of the YRDS fault (N65 E) and the orientation of the profile line in Figure 1 (N35°E), the shortening rate across the Daxue Shan is 2.2 ± 0.2 mm/year.

By summing up the shortening values obtained on timescales of 10^4–10^5 years for the range-bounding thrust faults along the western Qilian Shan (mean value: 1.6 ± 0.2 mm/year), the central Daxue Shan (2.2 ± 0.2 mm/year), and the Danghe Nan Shan (1–1.5 or 1.25 ± 0.25 mm/year), we obtain a total value of 5.1 ± 0.4 mm/year. This value is identical within error to the GPS-based shortening rate of 5.2 ± 0.3 mm/year along the 350-km-long profile line extending from the Hexi Corridor to the western Qaidam Basin (Figure 1) and agrees with the shortening rate of 5.5 ± 1.5 mm/year obtained by Zhang et al. (2004) using older GPS data. Farther east along a N30°E-trending profile across the central Qilian Shan, a slightly higher GPS-based shortening rate of 7.9 ± 1.9 mm/year has been reported by Zhong et al. (2020). The similarity between the millennial shortening rate and the GPS-derived rates suggests that most of the contractional strain in northern Tibet is taken up by fold-and-thrust systems along the major mountain ranges. Other faults such as the left-lateral Changma strike-slip fault (Figure 1) and thrust faults located in the Hexi Corridor are only responsible for minor amounts of crustal shortening (Hetzel et al., 2002; Liu et al., 2017b; Zheng et al., 2013a,b).

Near the town of Subei, the slip rate of the Altyn-Tagh strike-slip fault decreases from ~11–9 mm/year to ~7–5 mm/year (Xu et al., 2005; Zhang et al., 2007). The transfer of this left-lateral slip on thrust faults in the northwesternmost Danghe Nan Shan explains the high shortening rate of 5.5 ± 1.5 mm/year in this part of the mountain belt (van der Woerd et al., 2001). However, east of the junction with the left-lateral Yema River–Daxue Shan (YRDS) strike-slip fault, the rate of thrust faulting along the Danghe Nan Shan must decrease significantly, because the YRDS fault (which has a millennial slip rate of ~2.5 mm/year as explained above), transfers about half of the shortening to the range-bounding thrust fault of the Daxue Shan (Figure 1). This transfer of slip by the YRDS strike-slip fault explains the difference in shortening rate between the westernmost Danghe Nan Shan south of Subei and our study area in the central part of the mountain range.

6. Conclusions

At the front of the Danghe Nan Shan mountain range in the NE Tibet, folded terraces constitute excellent geomorphic markers that enabled us to reconstruct the subsurface geometry of the underlying thrust fault. Using ^{10}Be exposure ages for a widely preserved terrace level and uplift values derived from a high-resolution DEM, we quantified the vertical slip rate of the Danghe Nan Shan frontal thrust during the last ~80 ka as 0.6 ± 0.2 mm/year. The shortening rate associated with this thrust fault is 0.7–0.8 mm/year and was determined based on the assumption that the cross-sectional area of the fault-related fold was preserved during deformation. Adding the shortening rate that we tentatively inferred for the more steeply dipping thrust fault in the piedmont of the Danghe Nan Shan results in a shortening rate of 1.0–1.5 mm/year across

the entire mountain range. This estimate is in good agreement with the rate of elastic strain accumulation recorded by GPS data, if one assumes that the two thrust faults take up the interseismic strain that accumulates in a 60–100-km-wide region. The consistency between decadal and millennial shortening rates is also evident for the entire region of northern Tibet, where the GPS-based shortening rate of ~5 mm/year between the Qaidam Basin and the Hexi Corridor is the same as the one obtained by adding up the slip rates of the thrust faults extending along the three largest mountain ranges. The observed shortening at the margin and in the interior of the northern Tibetan Plateau is kinematically linked to the eastward decrease in the slip rate of the Altyn Tagh fault.

Data Availability Statement

Supplementary data of this study (Table S1, Figure S1) are provided in the supporting information (https://doi.org/10.1029/2020TC006584). The topographic profiles, the ^{10}Be data, and the GPS data (Gan et al., 2007; Wang and Shen, 2020) are stored in the PANGAEA Data Publisher (Xu et al., 2021) (https://doi.org/10.1594/PANGAEA.927853).

Acknowledgments
We are indebted to Ryan Gold for kindly generating the digital elevation model used in this study. We thank A. Niehus for her help during preparation of the ^{10}Be samples and the team of Cologne AMS for the timely analysis of all samples. We gratefully acknowledge funding for fieldwork, sample preparation, and AMS analyses provided by the Leibniz Universität Hannover (start-up funds to A. Hampel) and the Alexander von Humboldt Foundation (1-year fellowship awarded to Q. Xu). We thank Taylor Schildgen for editorial handling and the Associate Editor, Laura Gregory, and an anonymous reviewer for their comments, which helped to improve the manuscript.

References

Ader, T., Avouac, J.-P., Liu-Zeng, J., Lyon-Caen, H., Bollinger, L., Galetzka, J., et al. (2012). Convergence rate across the Nepal Himalaya and interseismic coupling on the Main Himalayan Thrust: Implications for seismic hazard. *Journal of Geophysical Research: Solid Earth*, *117*, B04403. https://doi.org/10.1029/2011JB009071

Anderson, R. S., Repka, J. L., & Dick, G. S. (1996). Explicit treatment of inheritance in dating depositional surfaces using in situ ^{10}Be and ^{26}Al. *Geology*, *24*, 47–51.

Balco, G., Stone, J. O., Lifton, N. A., & Dunai, T. J. (2008). A complete and easily accessible means of calculating surface exposure ages or erosion rates from ^{10}Be and ^{26}Al measurements. *Quaternary Geochronology*, *3*, 174–195. https://doi.org/10.1016/j.quageo.2007.12.001

Binnie, S. A., Dewald, A., Heinze, S., Voronina, E., Hein, A., Wittmann, H., et al. (2019). Preliminary results of CoQtz-N: A quartz reference material for terrestrial in-situ cosmogenic ^{10}Be and ^{26}Al measurements. *Nuclear Instruments and Methods in Physics Research B*, *456*, 203–212. https://doi.org/10.1016/j.nimb.2019.04.073

Borchers, B., Marrero, S., Balco, G., Caffee, M., Goehring, B., Lifton, N., et al. (2016). Geological calibration of spallation production rates in the CRONUS-Earth project. *Quaternary Geochronology*, *31*, 188–198. https://doi.org/10.1016/j.quageo.2015.01.009

Brown, E. T., Bourlès, D. L., Burchfiel, B. C., Deng, Q., Li, J., Molnar, P., et al. (1998). Estimation of slip rates in the southern Tien Shan using cosmic ray exposure dates of abandoned alluvial fans. The *Geological Society of America Bulletin*, *110*, 377–386.

Chevalier, M.-L., Van der Woerd, J., Tapponnier, P., Haibing, L., Ryerson, F. L., & Finkel, R. C. (2016). Late Quaternary slip-rate along the central Bangong-Chaxikang segment of the Karakorum fault, western Tibet. The *Geological Society of America Bulletin*, *128*, 284–314. https://doi.org/10.1130/B31269.1

Cording, A., Hetzel, R., Kober, M., & Kley, J. (2014). ^{10}Be exposure dating of river terraces at the southern mountain front of the Dzungarian Alatau (SE Kazakhstan) reveals rate of thrust faulting over the past ~400 ka. *Quaternary Research*, *81*, 168–178. https://doi.org/10.1016/j.yqres.2013.10.016

Cowgill, E., Gold, R. D., Chen, X., Wang, X. F., Arrowsmith, J. R., & Southon, J. (2009). Low Quaternary slip rate reconciles geodetic and geologic rates along the Altyn Tagh fault, northwestern Tibet. *Geology*, *37*(7), 647–650. https://doi.org/10.1130/G25623A.1

Dewald, A., Heinze, S., Jolie, J., Zilges, A., Dunai, T., Rethemeyer, J., et al. (2013). CologneAMS, a dedicated center for accelerator mass spectrometry in Germany. *Nuclear Instruments and Methods in Physics Research Section B: Beam Interactions with Materials and Atoms*, *294*, 18–23. https://doi.org/10.1016/j.nimb.2012.04.030

Ellis, M. A., & Densmore, A. L. (2006). First-order topography over blind thrusts. In S. D. Willett, N. Hovius, M. T. Brandon, & D. Fisher (Eds.), *Tectonics, climate, and landscape evolution* (Vol. 398, pp. 251–266). Geological Society of America Special Paper. https://doi.org/10.1130/2006.2398(15

Gan, W., Zhang, P., Shen, Z. K., Niu, Z., Wang, M., Wan, Y., et al. (2007). Present-day crustal motion within the Tibetan Plateau inferred from GPS measurements. *Journal of Geophysical Research: Solid Earth*, *112*(B08416). https://doi.org/10.1029/2005JB004120

Gansu Geological Bureau. (1975). *Report of regional geological Survey, Yueyahu geological map, scale: 1: 200 000* (p. 140). Geological Publishing House (in Chinese).

Gold, R. D., Cowgill, E., Arrowsmith, J. R., Gosse, J., Chen, X., & Wang, X. F. (2009). Riser diachroneity, lateral erosion, and uncertainty in rates of strike-slip faulting: A case study from Tuzidun along the Altyn Tagh Fault, NW China. *Journal of Geophysical Research: Solid Earth*, *114*(B04401). https://doi.org/10.1029/2008JB005913

Gold, R. D., Cowgill, E., Arrowsmith, J. R., Chen, X., Sharp, W. D., Cooper, K. M., et al. (2011). Faulted terrace risers place new constraints on the late Quaternary slip rate for the central Altyn Tagh fault, northwest Tibet. The *Geological Society of America Bulletin*, *123*(5–6), 958–978. https://doi.org/10.1130/B30207.1

Hampel, A., & Hetzel, R. (2015). Horizontal surface velocity and strain patterns near thrust and normal faults during the earthquake cycle: The importance of viscoelastic relaxation in the lower crust and implications for interpreting geodetic data. *Tectonics*, *34*, 731–752. https://doi.org/10.1002/2014TC003605

Hetzel, R. (2013). Active faulting, mountain growth, and erosion at the margins of the Tibetan Plateau constrained by in situ-produced cosmogenic nuclides. *Tectonophysics*, *582*, 1–24. https://doi.org/10.1016/j.tecto.2012.10.027

Hetzel, R., Hampel, A., Gebbeken, P., Xu, Q., & Gold, R. D. (2019). A constant slip rate for the western Qilian Shan frontal thrust during the last 200 ka consistent with GPS-derived and geological shortening rates. *Earth and Planetary Science Letters*, *509*, 100–113. https://doi.org/10.1016/j.epsl.2018.12.032

Hetzel, R., Niedermann, S., Tao, M., Kubik, P. W., Ivy-Ochs, S., Gao, B., & Strecker, M. R. (2002). Low slip rates and long-term preservation of geomorphic features in Central Asia. *Nature*, *417*(6887), 428–432. https://doi.org/10.1038/417428a

Hu, X., Pan, B., Kirby, E., Gao, H., Hu, Z., Cao, B., et al. (2015). Rates and kinematics of active shortening along the eastern Qilian Shan, China, inferred from deformed fluvial terraces. *Tectonics*, *34*(12), 2478–2493. https://doi.org/10.1002/2015TC003978

Huang, W., Yang, X., Li, A., Thompson, J. A., & Zhang, L. (2014). Climatically controlled formation of river terraces in a tectonically active region along the southern piedmont of the Tian Shan, NW China. *Geomorphology*, *220*, 15–29. https://doi.org/10.1016/j.geomorph.2014.05.024

Li, T., Chen, J., Thompson Jobe, J. A., Burbank, D. W., Cheng, X., Xu, J., et al. (2018). Active bending-moment faulting: Geomorphic expression, controlling conditions, accommodation of fold deformation. *Tectonics*, *37*, 1–29. https://doi.org/10.1029/2018TC004982

Lifton, N., Sato, T., & Dunai, T. J. (2014). Scaling in situ cosmogenic nuclide production rates using analytical approximations to atmospheric cosmic-ray fluxes. *Earth and Planetary Science Letters*, *386*, 149–160. https://doi.org/10.1016/j.epsl.2013.10.052

Liu, R., Li, A., Zhang, S., Chen, Z., & Guo, C. (2017b). The Late Quaternary tectonic deformation revealed by the terraces on the Baiyang River in the northern Qilian Mountains. *Seismology and Geology*, *39*(6), 1237–1255.(in Chinese with English abstract). https://doi.org/10.3969/j.issn.0253-4967.2017.06.010

Liu, X., Yuan, D., & Su, Q. (2019). Late Pleistocene slip rate on a blind thrust in the western Qilian Shan, NW China. *Geomorphology*, *345*, 106841. https://doi.org/10.1016/j.geomorph.2019.106841

Liu, X. W., Yuan, D. Y., & Su, Q. (2017a). Late Pleistocene slip rate of the northern Qilian Shan frontal thrust, western Hexi Corridor, China. *Terra Nova*, *29*, 238–244. https://doi.org/10.1111/ter.12270

Luo, H., Wengui, H. E., Daoyang, Y., & Yanxiu, S. (2015). Slip rate of Yema River–Daxue Mountain Fault since the Late Pleistocene and its implications on the deformation of the northeastern margin of the Tibetan Plateau. *Acta Geologica Sinica - English Edition*, *89*(2), 561–574. https://doi.org/10.1111/1755-6724.12447

Marshall, S. T., Funning, G. J., & Owen, S. E. (2013). Fault slip rates and interseismic deformation in the western Transverse Ranges, California. *Journal of Geophysical Research: Solid Earth*, *118*. https://doi.org/10.1002/jgrb.50312

Meyer, B., Tapponnier, P., Bourjot, L., Métivier, F., Gaudemer, Y., Peltzer, G., et al. (1998). Crustal thickening in Gansu-Qinghai, lithospheric mantle subduction, and oblique, strike-slip controlled growth of the Tibet plateau. *Geophysical Journal International*, *135*(1), 1–47. https://doi.org/10.1046/j.1365-246X.1998.00567.x

Noh, M. J., & Howat, I. M. (2015). Automated stereo-photogrammetric DEM generation at high latitudes: Surface Extraction with TIN-based Search-space Minimization (SETSM) validation and demonstration over glaciated regions. *GIScience and Remote Sensing*, *52*, 198–217. https://doi.org/10.1080/15481603.2015.1008621

Reimer, P., Austin, W. E. N., Bard, E., Bayliss, A., Blackwell, P. G., Ramsey, C. B., et al. (2020). The IntCal20 Northern Hemisphere radiocarbon age calibration curve (0–55 CAL kBP). *Radiocarbon*, *62*(4), 725–757. https://doi.org/10.1017/RDC.2020.41

Repka, J. L., Anderson, R. S., & Finkel, R. C. (1997). Cosmogenic dating of fluvial terraces, Fremont River, Utah. *Earth and Planetary Science Letters*, *152*, 59–73.

Ritz, J. F., Bourlès, D., Brown, E. T., Carretier, S., Chéry, J., Enhtuvshin, B., et al. (2003). Late Pleistocene to Holocene slip rates for the Gurvan Bulag thrust fault (Gobi-Altay, Mongolia) estimated with ^{10}Be dates. *Journal of Geophysical Research*, *108*, 2162. https://doi.org/10.1029/2001JB000553

Saint-Carlier, D., Charreau, J., Lavé, J., Blard, P.-H., Dominguez, S., Avouac, J.-P., et al. (2016). Major temporal variations in shortening rate absorbed along a large active fold of the southeastern Tianshan piedmont (China). *Earth and Planetary Science Letters*, *434*, 333–348. https://doi.org/10.1016/j.epsl.2015.11.041

Seong, Y. B., Kang, H. C., Ree, J. H., Yi, C., & Yoon, H. (2011). Constant slip rate during the late Quaternary along the Sulu He segment of the Altyn Tagh Fault near Changma, Gansu, China. *Island Arc*, *20*, 94–106. https://doi.org/10.1111/j.1440-1738.2010.00743.x

Shao, Y., (2010). *The activity features during late quaternary of Yema River-Danghe Nan Shan Faults in Western Qilian Shan (Master dissertation)* (pp. 1–80), Lanzhou Institute of Seismology China Earthquake Administration. Retrieved from China National Knowledge Infrastructure, http://cdmd.cnki.com.cn/Article/CDMD-85403-1014240187.htm

Shao, Y., Yuan, D., Oskin, M. E., Wang, P., Liu-Zeng, J., Li, C., & Wu, Z. (2017). Historical (Yuan Dynasty) Earthquake on the North Danghe Nanshan Thrust, Western Qilian Shan. *Bulletin of the Seismological Society of America*, *107*(3), 1175–1184. https://doi.org/10.1785/0120160289

Shean, D. E., Alexandrov, O., Moratto, Z. M., Smith, B. E., Joughin, I. R., Porter, C., & Morin, P. (2016). An automated, open-source pipeline for mass production of digital elevation models (DEMs) from very-high-resolution commercial stereo satellite imagery. *ISPRS Journal of Photogrammetry and Remote Sensing*, *116*, 101–117. https://doi.org/10.1016/j.isprsjprs.2016.03.012

Stein, R. S., King, G. C. P., & Rundle, J. B. (1988). The growth of geological structures by repeated earthquakes 2. Field examples of continental dip-slip faults. *Journal of Geophysical Research*, *93*(4), 13,319–13,331. https://doi.org/10.1029/JB093iB11p13319

Styron, R., Taylor, M., & Okoronkwo, K. (2010). Database of Active Structures from the Indo-Asian Collision. *EOS Transactions AGU*, *91*, 181–182. https://doi.org/10.1029/2010EO200001

Tapponnier, P., & Molnar, P. (1977). Active faulting and tectonics in China. *Journal of Geophysical Research*, *82*, 2905–2930. https://doi.org/10.1029/JB082i020p02905

Taylor, M., Yin, A., Ryerson, F., Kapp, P., & Ding, L. (2003). Conjugate strike-slip faulting along the Bangong-Nujiang suture zone accommodates coeval east-west extension and north-south shortening in the interior of the Tibetan Plateau. *Tectonics*, *22*, 1044. https://doi.org/10.1029/2002TC001361

Thompson, S. C., Weldon, R. J., Rubin, C. M., Abdrakhmatov, K., Molnar, P., & Berger, G. W. (2002). Late Quaternary slip rates across the central Tien Shan, Kyrgyzstan, central Asia. *Journal of Geophysical Research*, *107*(B9), 2203. https://doi.org/10.1029/2001JB000596

Van der Woerd, J., Ryerson, F. J., Tapponnier, P., Gaudemer, Y., Finkel, R., Mériaux, A. S., et al. (1998). Holocene left-slip rate determined by cosmogenic surface dating on the Xidatan segment of the Kunlun fault (Qinghai, China). *Geology*, *26*, 695–698.

Van der Woerd, J., Xu, X., Li, H., Tapponnier, P., Meyer, B., Ryerson, F. J., et al. (2001). Rapid active thrusting along the northwestern range front of the Tanghe Nan Shan (western Gansu, China). *Journal of Geophysical Research*, *106*(B12), 30,475–30,504. https://doi.org/10.1029/2001JB000583

Wang, M., & Shen, Z. K. (2020). Present-day crustal deformation of continental China derived from GPS and its tectonic implications. *Journal of Geophysical Research*, *125*, e2019JB018774. https://doi.org/10.1029/2019JB018774

Wang, Y., Oskin, M. E., Zhang, H., Li, Y., Hu, X., & Lei, J. (2020). Deducing crustal-scale reverse-fault geometry and slip distribution from folded river terraces, Qilian Shan, China. *Tectonics*, *39*(1), e2019TC005901. https://doi.org/10.1029/2019TC005901

Xiong, J., Li, Y., Zhong, Y., Lu, H., Lei, J., Xin, W., et al. (2017). Latest Pleistocene to Holocene thrusting recorded by a flight of strath terraces in the eastern Qilian Shan, NE Tibetan Plateau. *Tectonics*, *36*, 2973–2986. https://doi.org/10.1002/2017TC004648

Xu, Q., Hetzel, R., Hampel, A., & Wolff, R. (2021). Topographic data, ^{10}Be data, and GPS data used in the study on the Danghe Nan Shan thrust fault. *PANGAEA*. https://doi.org/10.1594/PANGAEA.927853

Xu, X., Wang, F., Zheng, R., Chen, W., Ma, W., Yu, G., et al. (2005). Late quaternary sinistral slip rate along the Altyn Tagh fault and its structural transformation model. *Science in China - Series D: Earth Sciences*, *48*(3), 384–397. https://doi.org/10.1360/02yd0436

Yang, H., Yang, X., Huang, X., Li, A., Huang, W., & Zhang, L. (2018). New constraints on slip rates of the Fodongmiao-Hongyazi fault in the Northern Qilian Shan, NE Tibet, from the ^{10}Be exposure dating of offset terraces. *Journal of Asian Earth Sciences*, *151*, 131–147. https://doi.org/10.1016/j.jseaes.2017.10.034

York, D. (1966). Least square fitting of a straight line. *Canadian Journal of Physics*, *44*, 1079–1086.

Zhang, P. Z., Shen, Z., Wang, M., Gan, W., Bürgmann, R., Molnar, P., et al. (2004). Continuous deformation of the Tibetan Plateau from global positioning system data. *Geology*, *32*, 809–812. https://doi.org/10.1130/G20554.1

Zhang, P. Z., Molnar, P., & Xu, X. (2007). Late Quaternary and present-day rates of slip along the Altyn Tagh Fault, northern margin of the Tibetan Plateau. *Tectonics*, *26*(5). https://doi.org/10.1029/2006TC002014

Zheng, W., Zhang, P., He, W., Yuan, D., Shao, Y., Zheng, D., et al. (2013a). Transformation of displacement between strike-slip and crustal shortening in the northern margin of the Tibetan Plateau: Evidence from decadal GPS measurements and late Quaternary slip rates on faults. *Tectonophysics*, *584*, 267–280. https://doi.org/10.1016/j.tecto.2012.01.006

Zheng, W. J., Zhang, H. P., Zhang, P. Z., Molnar, P., Liu, X. W., & Yuan, D. Y. (2013b). Late Quaternary slip rates of the thrust faults in western Hexi Corridor (Northern Qilian Shan, China) and their implications for northeastward growth of the Tibetan Plateau. *Geosphere*, *9*(2), 342–354. https://doi.org/10.1130/GES00775.1

Zhong, Y., Xiong, J., Li, Y., Zheng, W., Zhang, P., Lu, H., et al. (2020). Constraining Late Quaternary crustal shortening in the eastern Qilian Shan from deformed river terraces. *Journal of Geophysical Research: Solid Earth*, *125*, e2020JB020631. https://doi.org/10.1029/2020JB020631